Astron. Astrophys. 95, 250–265 (1981)

ASTRONOMY AND ASTROPHYSICS

Multifrequency Observations of Very Large Radio Galaxies

III: NGC 315

A. G. Willis[1], R. G. Strom[2], A. H. Bridle[3], and E. B. Fomalont[4]

[1] Netherlands Foundation for Radio Astronomy, Radiosterrenwacht Westerbork, 9433 TA Zwiggelte, The Netherlands
[2] Netherlands Foundation for Radio Astronomy, Radiosterrenwacht Dwingeloo, 7991 PD Dwingeloo, The Netherlands
[3] Department of Physics*, Queen's University at Kingston, Kingston, Ontario K7L 3N6, Canada
[4] National Radio Astronomy Observatory, Edgemont Road, Charlottesville, Va. 22901, USA

Received September 22, accepted November 12, 1980

Summary:

Observations at 49 cm and 21 cm of the total and polarized intensities of the jets and extended lobes in the large radio galaxy NGC 315 are presented. The dominant component of the magnetic field in both the main and counter jets is well organized and is oriented perpendicular to the extension of the jets over most of their length. The degree of polarization, P, of the jet emission increases with distance from the central radio core, indicating an increasingly ordered magnetic field within the jets. Over the main jet the depolarization, P_{49}/P_{21}, is roughly constant at about 0.8±0.2 everywhere. There is evidence for fluctuations of 8–10 rad m^{-2} in the rotation measure of the foreground galactic Faraday screen over the area covered by the source. The 49 cm – 21 cm spectral index of the jets is constant at $\alpha = -0.6$ ($S_\nu \propto \nu^\alpha$).

The main jet does not expand at a constant rate, and a combination of intensity and lateral expansion properties is used to characterize six different regimes in order of distance from the central core. Inner regimes of rapid expansion are followed by regimes of lateral confinement and apparently free expansion respectively. These differing regimes also correspond to different dependencies of the surface brightness upon the cross-sectional width of the jet.

Key words: radio galaxies – linear polarization – magnetic fields – radio jets.

1. Introduction.

This is the third in a series of papers presenting multi- frequency radio observations of very large radio galaxies using the Westerbork Synthesis Radio Telescope (WSRT). Papers I (Willis and Strom, 1978) and II (Strom and Willis, 1980) discussed the sources 3C326 and 3C236 respectively. Here we describe observations of NGC 315 (DW0055+30). This source was shown by Bridle et al. (1976, 1979) to have an angular size of ∿58 arcmin, which at the redshift of NGC 315 (0.0167; Colla et al., 1975) corresponds to an intrinsic projected size of ∿1.1 Mpc ($H = 75$ km s^{-1} Mpc^{-1}).

DW0055+30 was first detected by Davis (1967) in a 1400 MHz continuum survey with the 25 meter paraboloid at the Dwingeloo Radio Observatory. The first hint of large scale structure was revealed in the NRAO 300 ft telescope survey by Bridle et al. (1972) at 1400 MHz. Further observations by Bridle et al. (1976, 1979) showed that the source contains highly collimated radio jets connecting a compact radio core near the nucleus of the galaxy to an unusual Z-shaped configuration of outer radio lobes. The regions where the jets emerge from the central part of the galaxy were examined at high resolution by Bridle et al. (1979) and by Fomalont et al. (1980) using data at 1465 and 4885 MHz from the Very Large Array (VLA). These observations showed that the dominant component of the magnetic field in the brighter jet is parallel to the jet within 20" (6.3 kpc) of the radio core but becomes perpendicular to the extension of the jet beyond this distance, much as had been predicted in continuous-beam models for filled jets (Blandford and Rees, 1974).

We have used the WSRT to map the large scale distribution of total intensity and polarization in NGC 315 at wavelengths of 49 and 21 cm. At 49 cm the half-power width of the WSRT primary beam is 81 arcmin so the entire radio source was easily contained within a single field of view. At 21 cm the primary beam half-power width is 36 arcmin so it was necessary to map the radio structure at this wavelength using two separate fields of view – one centered to the northwest of the central nuclear source and one centered on the southeast lobe. Full details of the observations are given in Table 1.

Table 1: Observing log for NGC 315.

Wavelength(cm)	Field center (1950.0) RA	DEC	Baselines(m)[a] Shortest	Longest	Excluded (HA)	Date
49 cm	$00^h55^m04^s.4$	$30^\circ05'09''.0$	72	1440	-	1976.1
	00 55 04.4	30 05 09.0	36	1404	-	1976.1
21 cm	00 54 30.0	30 06 30.0	90	1458	-	1977.4
	"	"	54	1422	-	1977.5
	"	"	36	1404	-	1977.6
	00 57 15.0	29 50 00.0	72	1440	936,1008(4^h to 6^h)	1977.4
	"	"	90	1458	-	1977.4
	"	"	54	1422	-	1977.5
	"	"	36	1404	-	1977.5
	"	"	936	1008		1977.9[b]

a) Intermediate baselines at an interval of 72 m are included between the shortest and longest.

b) This observation only covers the range $+4^h$ to $+6^h$ in hour angle.

* Present address: National Radio Astronomy Observatory, VLA Program, P. O. Box 0, Socorro, New Mexico 87801, USA, and Dept. of Physics and Astronomy, University of New Mexico, Albuquerque, New Mexico 87131, USA

Send offprint requests to: A. G. Willis

The data were processed through the standard WSRT reduction package (Högbom and Brouw, 1974; Van Someren Gréve, 1974). To remove the effects of grating rings and near-in sidelobes, the Fourier transformed maps were decomposed into point source components using the CLEAN algorithm (Högbom, 1974) and were then restored by convolving the point source distributions with the central part of the synthesized antenna pattern.

The 49 cm polarization data (Figs. 1B, 1C and 1D) have been corrected for ionospheric Faraday rotation by the following procedure (Strom, 1972). Values of the critical frequency f_0F2 obtained on an hourly basis from the De Bilt ionosonde station and the average slab thickness appropriate for the time when the measurement was made are used to produce estimates of total electron density. These are combined with a model for the geomagnetic field to derive position angle corrections as a function of azimuth and elevation which are then applied to the Westerbork data. The 49 cm observations of NGC 315 were made at the minimum of solar activity so that, although they began just before noon, the correction was generally small. Apart from several hours when values of 25° to 35° were recorded it was usually 15° or less. The residual error due to the ionosphere in the 49 cm electric vector position angles is estimated to be $\pm$ 5°.

2. Results.

a) 49 cm wavelength.

A 49 cm total intensity map was published by Bridle et al. (1979); for completeness we reproduce that map in Fig. 1A. Figs. 1B and 1C show the corresponding distributions of polarized flux density and E-vector position angle and Fig. 1D shows the map of the degree of polarization P = (100 x $(Q^2+U^2)^{\frac{1}{2}}$/I).

These figures show that NGC 315 is significantly polarized at this long wavelength. In this respect the source is very similar to the other giant radio galaxies 3C326 and 3C236 studied in papers I and II.

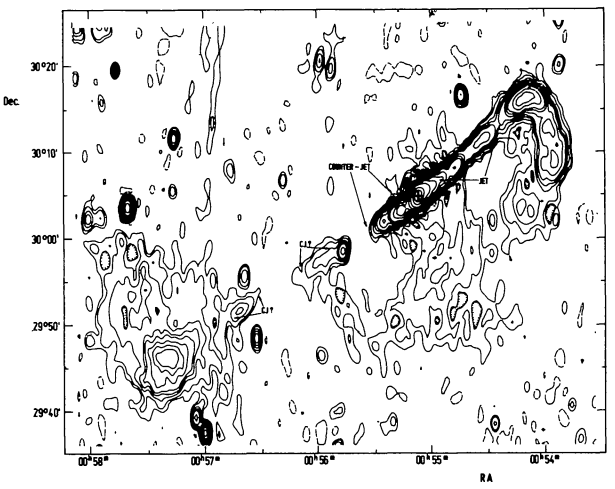

Fig. 1A: A Westerbork 610 MHz total intensity map of the radio emission associated with NGC 315 (reproduced from Bridle et al., 1979). The resolution (FWHM) is 55" (α) by 110" (δ). Contours are at -5 (dashed), 2.5, 5, 10, 15, 20, 30, 40, 50, 75, 100, 150, 250, 500, 750, 1000 mJy/beam A cross marks the position of the center of the galaxy.

A striking feature is the variation in the degree of linear polarization along the main and counter jets (see Fig. 1D). We shall call the jet extending from the central radio core to the northwest the main jet because of its higher surface brightness, and that stretching to the southeast the counter jet. The degree of polarization systematically increases with distance from the radio core in both jets (see Figs. 1D and 6). The degree of polarization in the main jet increases steadily to ∿28 to 30% at a distance of ∿216" (∿68 kpc) from the core, then remains roughly constant (within the uncertainty) near this value until ∿430" (∿135 kpc) from the core where it again begins to increase, reaching ∿40% by a distance of ∿510" (∿160 kpc). This value holds for a further 140" (44 kpc) at which point the degree of polarization climbs again, attaining a maximum value of ∿50% at a distance of ~700 arcsec (∿220 kpc). Beyond this distance the degree of polarization drops sharply to about 15% at the inner edge of the brightness peak at the end of the jet. It decreases further, to ∿5%, in the center of the peak but begins to rise again near its outer edge.

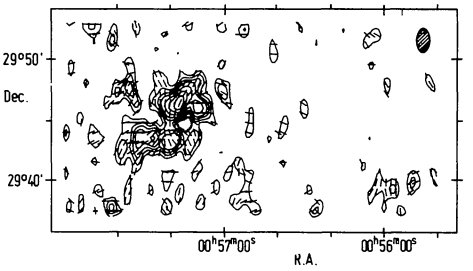

Fig. 1B: A contour map of the polarized flux density from the southeast lobe of NGC 315 at 610 MHz. The contours are at 3, 4.5, 6, 7.5, 10, 12.5, 15 mJy/beam. The superimposed lines indicate the position angles of the electric vectors.

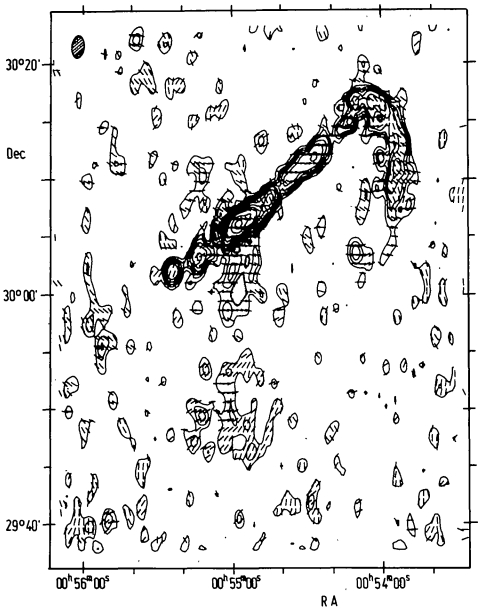

Fig. 1C: A contour map of the polarized flux density from the jet and northwest lobe of NGC 315 at 610 MHz. The contours are at 2.5, 4, 5.5, 7.5, 10, 15, 20, 25, 35, 45 mJy/beam. The superimposed lines indicate the position angles of the electric vectors.

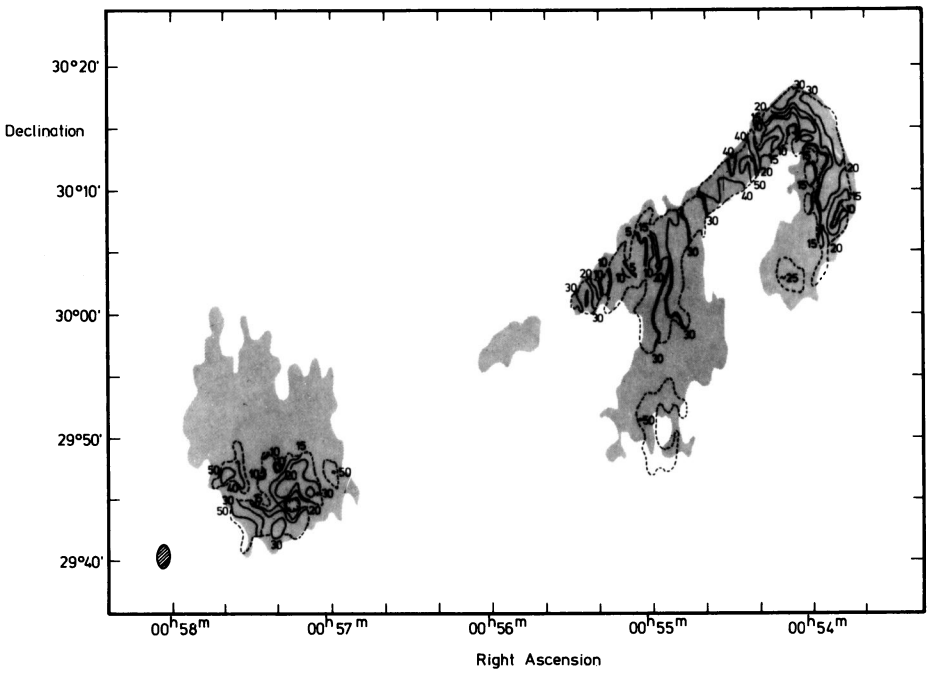

Fig. 1D: Contours of the degree of linear polarization at 610 MHz superimposed upon a gray shading which corresponds to the 5 mJy contour of Fig. 1A.

A similar but less rapid increase in the degree of polarization is evident in the counter jet. (Fig. 1D and 6). A degree of polarization of 30% is attained in this jet at a distance of ∿ 265" (∿83 kpc) as opposed to 216" for the main jet. The maximum degree of polarization in the counter jet is ∿40%.

No significant polarized flux was detected at 49 cm from either of the features labelled CJ ? (= counter jet ?) in Fig. 1A; this result places upper limits of 40% and 20% on the degree of polarization in the CJ ? features closer to and farther from the nucleus respectively.

Significantly polarized flux, corresponding to a degree of polarization which varies between ∿10 and ∿20%, is detected in the main peak of the southwest lobe. The polarization rises to higher values (∿40 to 50%) at the outer southeastern edge of the lobe. No significant polarized flux, corresponding to a limit in the degree of polarization of $\leqslant$ 30%, is detected from the diffuse emission stretching to the north away from the bright peak in the total intensity map.

The radio core itself is unpolarized at 49 cm (< 1%).

In general we find (see Fig. 6) that increases in the degree of polarization are correlated with decreases in the total intensity and vice versa, i.e. the polarized intensity is more constant than is the total intensity. At the maximum of the polarized brightness (∿50 mJy/ beam) the total intensity brightness is ∿225 mJy/beam (which yields a degree of polarization of ∿22%). At the location where the degree of polarization in the jet has risen to ∿50%, the polarized brightness is 15 mJy/beam while the total intensity brightness is 30 mJy/beam. Thus while the total intensity brightness has varied by a factor 7.5, the polarized brightness has varied by only a factor 3.3.

A similar situation holds for the northwest lobe (the feature oriented in PA ∿19°) at the end of the main jet. Examination of Figs. 1A and 1D shows again that maxima in the degree of polarization are generally associated with total intensity minima. Here, however, the degree of polarization has values ranging between ∿5 and 25%, generally lower than for the straight jet regime near the nucleus, but comparable to that in the peak of the southeast lobe.

b) 21 cm wavelength.

Figures 2A to 2H display maps of the total intensity and polarization of NGC 315 at 21 cm. The main and counter jets (Fig. 2A) have a complex morphology with a number of sub-peaks of emission, which are not placed symmetrically with respect to the central nuclear source. The structure in the map near the central nuclear source agrees well with that in the higher-resolution 20 cm VLA map published by Bridle et al. (1979). In particular, one can see that while the jet and counter jet are on average fairly straight, there is a slight but distinct oscillation in the ridge line joining the maximum brightness features. Two properties of the oscillation are of interest: a) it is not particularly periodic, and b) in so far as one can note a symmetry between the oscillations in the main and counter jets, the symmetry is rotational rather than mirror as in the jets of 3C449 (Perley et al., 1979).

An additional rough symmetry between the main and counter jets may be present. At a distance of ∿330 arcsec (104 kpc) from the core the brightness of the counter jet falls below our detection limit; at a similar distance to the northwest of the nucleus (∿380 arcsec) the main jet drops sharply in brightness by a factor of ∿2.5. This distance also corresponds to changes in the mean direction and collimation of the main jet.

There is a change in the average position angle of the main jet at about this location from a position angle of ∿127.5° to ∿135° (in the direction away from the core) and at distances beyond this location the cross-sectional width of the jet begins to increase rapidly (see sect. 4).

The 21 cm degrees of polarization appear to be even higher than those measured at 49 cm. In the main jet, nominal values as high as ∿70% are recorded (see Fig. 2D). The high values of ∿70% ± 25% recorded in the parts of the main jet between $\alpha = 00^h54^m16^s$ and $\alpha = 00^h54^m30^s$ may be systematically high for two reasons.

a) The polarized brightness in this part of the jet as well as in the northwest lobe is only ∿2.5 times the rms noise. Thus the most probable true degree of

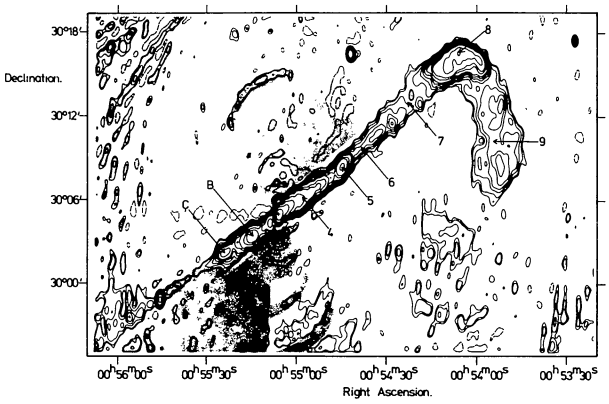

Fig. 2A: The jets and northwest lobe of NGC 315 as seen at 1415 MHz in total intensity by the WSRT. The resolution is 23" (α) x 46" (δ). Contours are at -2 (dashed), 0.6, 1, 2, 3, 4, 5, 6, 8, 10, 15, 20, 40, 80, 160, 320 mJy/beam. The numbers 4 through 9 and letters B and C refer to regions whose properties are given in Tables 3 and 4. Gray shaded regions are thought to be affected by instrumental responses. A cross marks the position of the center of the galaxy.

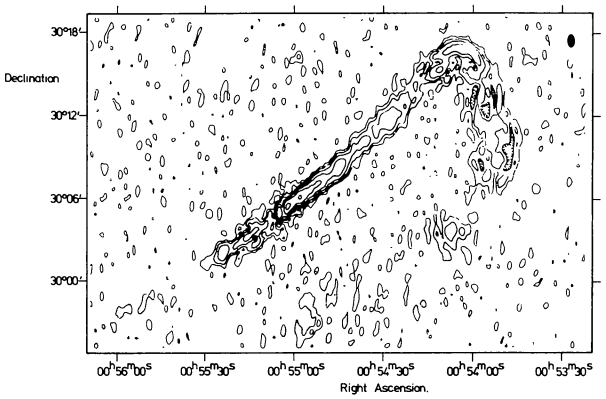

Fig. 2B: The 1415 MHz polarized flux density from the jets and the northwest lobe superimposed upon gray shading corresponding to the 0.6 mJy/beam contour of Fig. 2A. Contours are at 0.5, 1, 2, 4, 8, 16 mJy/beam.

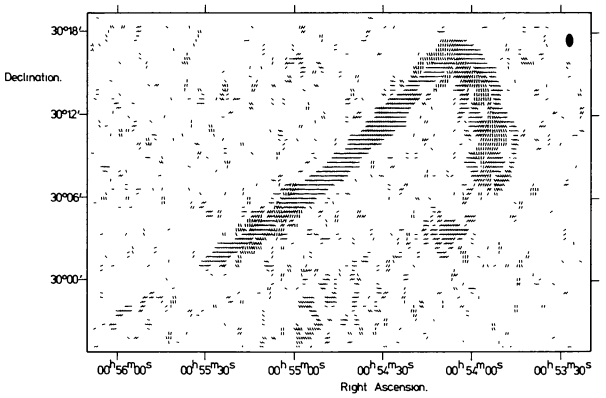

Fig. 2C: The 1415 MHz polarization E-vectors from the jets and northwest lobe superimposed upon gray shading corresponding to the 0.6 mJy/beam contour of Fig. 2A.

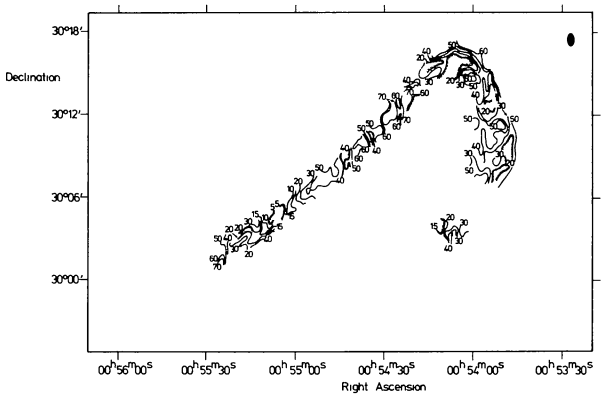

Fig. 2D: The 1415 MHz degree of polarization map of the jets and northwest lobe superimposed upon gray shading corresponding to the 0.6 mJy/beam contour of Fig. 2A.

polarization is ∿10% lower than the observed polarization since we are dealing with a signal whose probability distribution in the presence of noise is given by the Rice distribution (Vinokur, 1965; Wardle and Kronberg, 1974).

b) There is a significant non-uniform zero level offset that is typically 0.5 mJy in the total intensity map in the sense that the measured values of total intensity are too low. This causes the degree of polarization to appear too high. The true maxima are probably between 50 and 60%, the values found in the convolved maps (discussed below) where the brightness sensitivity is greater.

There is generally little evidence of a variation in the degree of polarization across the main jet; instead the variation seems to be mainly a function of position along the jet. In the counter jet the situation may be more complicated; in the region within 2.9 arcmin distance of the core, there is evidence of an increase in the degree of polarization toward the edges of the jet.

The 21 cm degrees of polarization P_{21} probably represent intrinsic values for the polarization of the jets unaffected by internal Faraday depolarization (although the values of P_{21} in those parts of the jet near the core may be affected by beam depolarization) because

a) the degrees of polarization in the outer parts of the jets are very high, and,

b) the VLA observations of the innermost 60 arcsec of the main jet (where Faraday depolarization should be highest) show the degree of polarization there to be only ∿10% even at 6 cm. This value is not very different from those found in the present observations.

While P_{21} in the bright peak of the northwest lobe (where the jet sharply bends towards the southwest) is only ∿20% it increases sharply toward the extreme northwest outer edge of the lobe, where values in excess of 60% occur. Values of P near 50% are also found at the western and southern edges of the northwest lobe.

There is also considerable polarization in the southeast lobe (Figs. 2F and 2H). The degree of polarization in the total intensity peak is ∿30% but P_{21} increases to values greater than 70% in the direction toward the southeast outer edge of the lobe. Convolution of the 21 cm full resolution map to the λ= 49 cm resolution yields a convincing detection of polarized flux from the region of lower surface

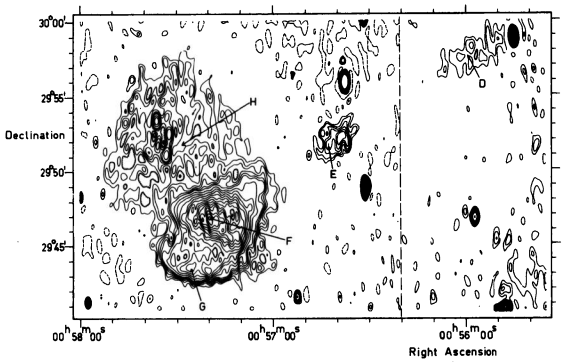

Fig. 2E: The southeast lobe and CJ? features of NGC 315 in total intensity at 1415 MHz. The resolution is 23" (α) x 46" (δ). Contours are at -0.75 (dashed), 0.25, 0.5, 0.75, 1, 1.25, 1.5, 2, 2.5, 3, 3.5, 4, 4.5, 5, 5.5, 6, 6.5, 7, 7.5, 8, 8.5 mJy/beam. In the region to the west of $\alpha = 00^h56^m20^s$ we have only drawn every second contour beginning at 0.5 mJy/beam, since the correction for primary beam attenuation significantly increases the noise at large distances from the field center. The letters D through H refer to regions whose properties are given in tables 3 and 4.

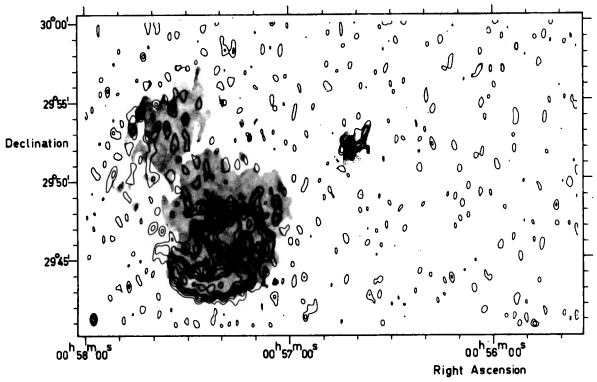

Fig. 2F: The 1415 MHz polarized flux density from the southeast lobe superimposed upon gray shading corresponding to the 0.5 mJy/beam contour of Fig. 2E. Contours are at 0.4, 0.6, 0.8, 1, 1.25, 1.5, 2, 2.5 mJy/beam.

brightness to the north of the central peak with P_{21} between 20 to 30%.

In the full resolution maps significant polarized flux is detected in the CJ? feature further from the radio core. In the lower surface brightness part of this feature at $\alpha \sim 00^h56^m42^s$ P_{21} reaches 75 ± 20% but drops to ∿40% on the higher surface brightness peak located at $\alpha \sim 00^h56^m38.5^s$. Since there is no polarized flux detected from especially the southern part of this CJ? feature (Fig. 2F), it is not surprising that when the 21 cm data are convolved to the 49 cm resolution, the observed degree of polarization drops to ∿30%. When the 21 cm data are convolved to the 49 cm resolution, a degree of polarization of ∿25% is detected at the CJ? feature closer to the radio core.

The 21 cm map of the southeast lobe (Fig. 2E) shows several compact features which lie adjacent to or are contained within the extended emission which we presume to be from NGC 315. We have attempted to determine whether these compact features are associated with NGC 315 or are unrelated background sources.

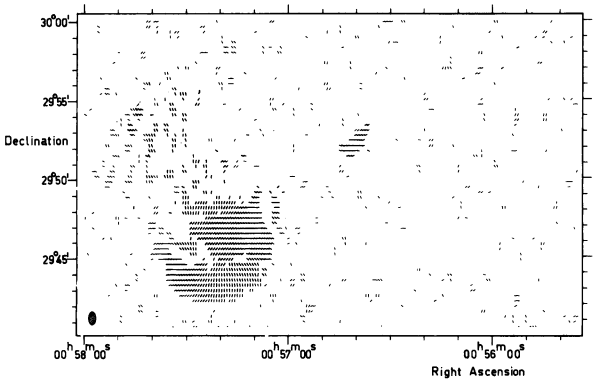

Fig. 2G: The 1415 MHz polarization E-vectors from the southeast lobe superimposed upon gray shading corresponding to the 0.5 mJy/beam contour of Fig. 2E.

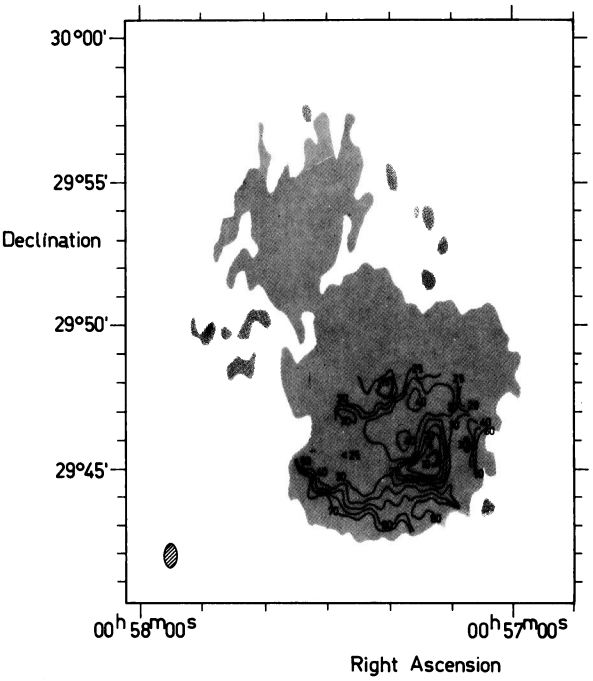

Fig. 2H: The 1415 MHz degree of polarization map of the southeast lobe superimposed upon gray shading corresponding to the 0.5 mJy/beam contour of Fig. 2.

The most interesting of these compact features is the source at $\alpha = 00^h55^m44.78^s$, $\delta = 29°58'50.9"$ (1950) which lies at the northwest edge of the CJ? feature nearer the nucleus. (The source also appears in the 49 cm map (Fig. 1A) where it is partially blended with the CJ? feature because of the lower 49 cm resolution.) Because of the relatively good alignment of this source with the over-all axis of the counter jet (the position angle of the source with respect to the nucleus is 125.7°, while that of the jet is ∿122°) we investigated the optical field in the vicinity of the source with the aid of deep III a-J and III a-F plates taken by A.G. de Bruyn at the Palomar 48-inch Schmidt telescope. The radio source coincides to within 0.6 arcsec in both coordinates with a $m_b \sim 21.5$ object that appears stellar. The object is brighter on the III a-J than on the III a-F plate and thus would seem relatively blue in colour. It has a radio spectral index of -1 (S_{49}= 35 mJy, S_{21}= 15 mJy).

While this spectrum is slightly steeper than that of the average extra-galactic radio source, the 49 cm flux density of the object may be high because of beam contamination from the adjacent CJ? feature and the present evidence suggests to us that the source may be a distant quasar physically unrelated to NGC 315. However, because of the discoveries in recent years of optical emission apparently associated with compact "hot spots" in the outer lobes of double radio sources (e.g. Saslaw et al., 1978) it may be worthwhile to obtain both optical spectra and a radio map of this object with better resolution to determine its nature. A finding chart is shown in Fig. 3.

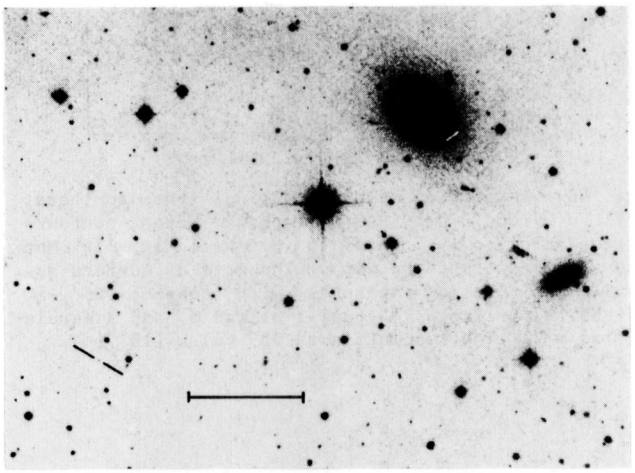

Fig. 3: A finding chart for the optical identification of the compact radio source located at $\alpha = 00^h55^m54.78^s$, $\delta = 29^\circ58'50.9"$ (1950). The optical counterpart is marked in the lower left hand corner. NGC 315 is the bright galaxy in the upper right part of the field. The bar marks a length of 3 arcmin. (Courtesy of A.G. de Bruyn).

There are also some compact sources located in the diffuse emission stretching to the northeast from the central peak in the southeast lobe. At least three sources are located in a group at $\alpha \sim 00^h57^m35^s$, $\delta \sim 29^\circ52'$. We have also examined the optical fields of these sources on the deep Schmidt plates obtained by De Bruyn, but no obvious optical counterparts exist. At present, there is little evidence either for or against the hypothesis that these sources are physically associated with the emission from NGC 315. The radio spectral index of this region (sect. 3b) is not significantly different from that in other parts of the southeast lobe.

3. Comparison of the 49 and 21 cm data.

We have used the 49 cm and 21 cm total intensity and polarization data to determine polarization, rotation measure and spectral index variations over the source. To make the appropriate comparisons we first convolved the 21 cm maps to the 49 cm resolution. We made the convolution as follows: we deleted all interferometer pairs having spacings longer than $\sim$620 meters (equal to the 49 cm maximum aperture in wavelengths) and then Fourier transformed the data using a Gaussian taper whose value dropped to 25% at 617 meters. The 49 cm and 21 cm maps were then CLEANED and restored with identical Gaussian beams having half intensity widths (FWHM) of 55" (α) x 110" (δ).

a) Polarization comparison.

We have used the polarization data at the two wavelengths
I) to determine the intrinsic orientation of the magnetic field over the radio galaxy and,
II) to study the depolarization between 21 and 49 cm wavelengths.

I. Magnetic field orientation.

To determine the intrinsic direction of the magnetic field within a radio galaxy, it is first necessary to correct the observed E-vectors for the effects of Faraday rotation within the radio galaxy itself and in the foreground interstellar medium of our own galaxy. Polarization data on NGC 315 are available at three wavelengths: our 49 and 21 cm mesurements and an 11 cm map at 4.5 arcmin resolution by Stoffel and Wielebinski (1978). Kronberg (private communication) has measured the rotation measures (RM) of several extragalactic radio sources within 20° of NGC 315. These RMs are mostly negative, with those sources lying closest to NGC 315 having RMs between -30 to -75 rad m^{-2}. We therefore fitted the Westerbork data with negative RMs and used the computed RMs and the Westerbork 21 cm E-vectors to predict 11 cm E-vector position angles for comparison with the 11 cm data of Stoffel and Wielebinski (1978). Consistency between all three wavelengths was obtained using RMs typically within a few radians m^{-2} of -80 rad m^{-2}, except over the "tail" of the northwest lobe at $\alpha \sim 00^h54^m10^s$, $\delta \sim 30^\circ03'$ (1950). Here we could not achieve a consistent fit with the 11 cm data using RMs of either -82 rad m^{-2} or (shifting the 49 cm - 21 cm position angle difference by πrad) -64 rad m^{-2}, which is the next lowest RM consistent with the WSRT data. In this region the observed 11 cm position angles lie approximately midway between those predicted by the two RMs. It is possible that our comparison might be confused in this region because the 11 cm resolution is 4.5 arcmin, much coarser than the WSRT resolution of 55" (α) x 110" (δ).

We therefore made RM maps from our 49 cm and 21 cm data with the assumption that individual RMs lie within $\pm$ 8 rad m^{-2} of -80 rad m^{-2} (this constraint is necessary to avoid position angle ambiguities of $n\pi$ when working with two frequencies) and that the RMs in the region at $\alpha \sim 00^h54^m10^s$, $\delta \sim 30^\circ03'$ were -82 rad m^{-2}.

Figures 4A and 4B show that the RM varies by up to $\sim$ 13 rad m^{-2} over NGC 315. Most of the variation in RM must be due to fluctuations in the foreground Faraday screen of our galaxy because the variation is much bigger than would be expected on the basis of the depolarization measurements of NGC 315 (see below). For instance, along the main and counter jets the RM varies by up to 11 rad m^{-2} (from -75 rad m^{-2} at the outer southeast edge of the counter jet to -86 rad m^{-2} at $\alpha \sim 00^h54^m45^s$, $\delta \sim 30\ 08'$). Over the same region, the depolarization is everywhere $\gtrsim$0.4, and on average $\sim$0.8. An average depolarization of 0.8 implies a Faraday depth at the back of the jet of $\sim$ 1.1 radians at 49 cm (see Burn, 1966) so we should expect an internal RM of no more than $\sim |1.1/2\lambda^2| = |2.3|$ rad m^{-2}. This is very small compared to the average RM over the jet of $\sim|80|$ rad m^{-2}. We might expect differences of $\sim 2x|2.3|$ rad m^{-2} between the jet and counter jet if, for example, the orientation of the magnetic field in the main jet was predominantly toward us and that in the counter jet was predominantly away from us, or vice versa. There is however no abrupt change in the RM at the division between counter jet and main jet. The

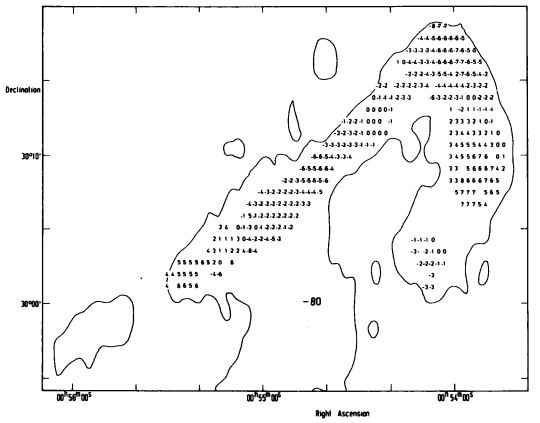

Fig. 4A: A rotation measure map of the jets and northwest lobe of NGC 315 superimposed on a contour corresponding to 4.5 mJy per beam at 610 MHz (Gaussian beam restored map). The grid of numbers are the local rotation measures relative to -80 radians m^{-2}, i.e. -2 equals -82 radians m^{-2} and 6 equals -74 radians m^{-2}. The resolution is 55" (α) x 110" (δ).

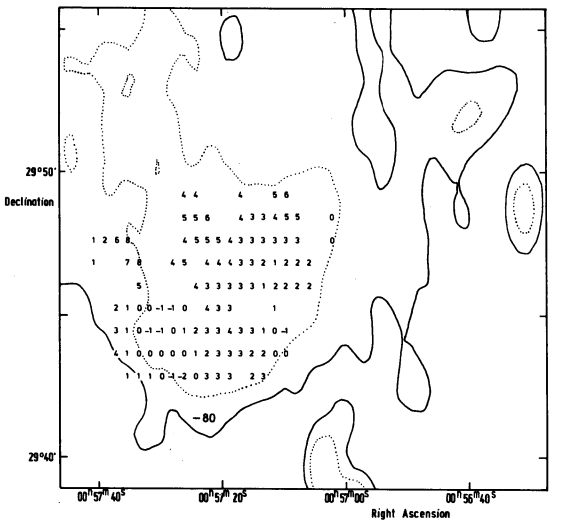

Fig. 4B: A rotation measure map of the southeast lobe of NGC 315 super-imposed upon contours corresponding to 4.5 and 15 mJy/beam at 610 MHz (Gaussian beam restored map). The grid of numbers are the local rotation measures with respect to -80 radians m^{-2}, i.e. -1 equals -81 rad m^{-2} and 3 equals -77 rad m^{-2}. The resolution is 55" (α) x 110" (δ).

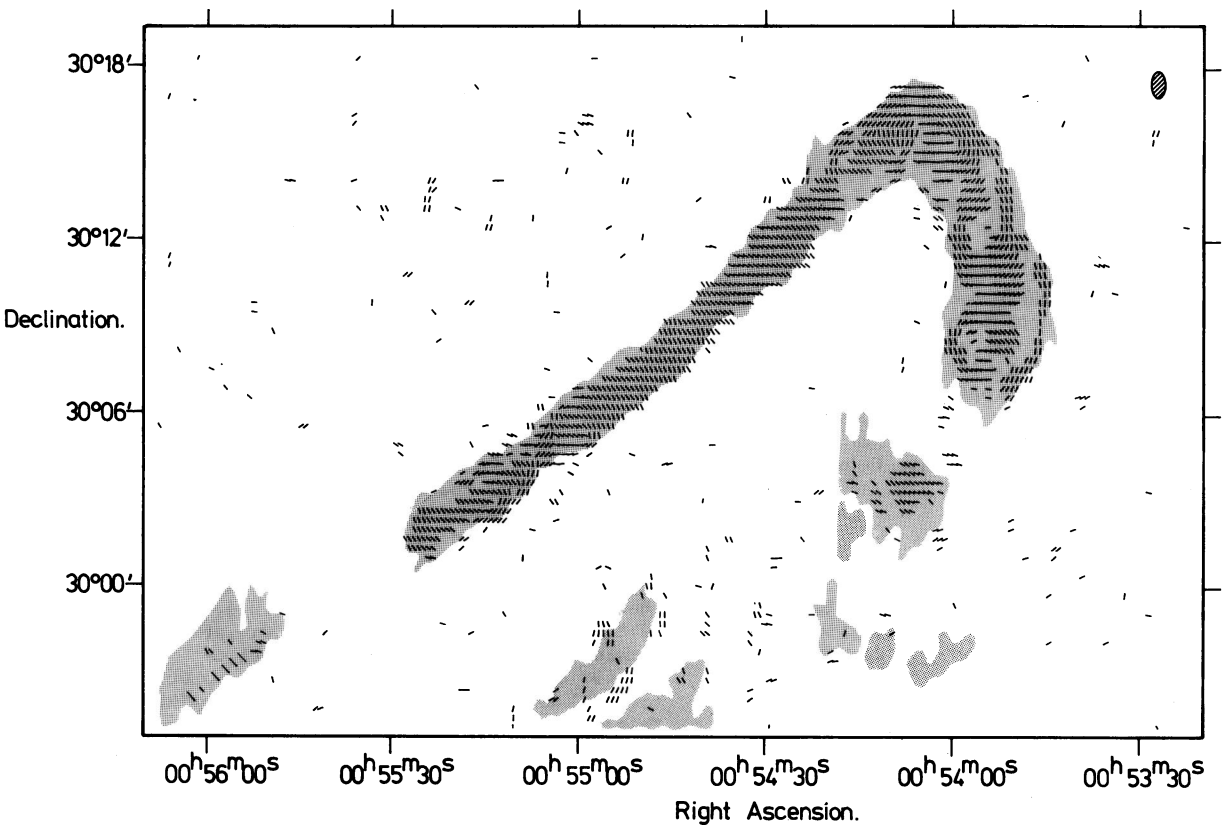

Fig. 5A: A high resolution (23"(α) x 46" (δ)) map of the magnetic field in the jets and northwest lobe of NGC 315 superimposed on gray shading corresponding to the 0.6 mJy per beam contour of Fig. 2A.

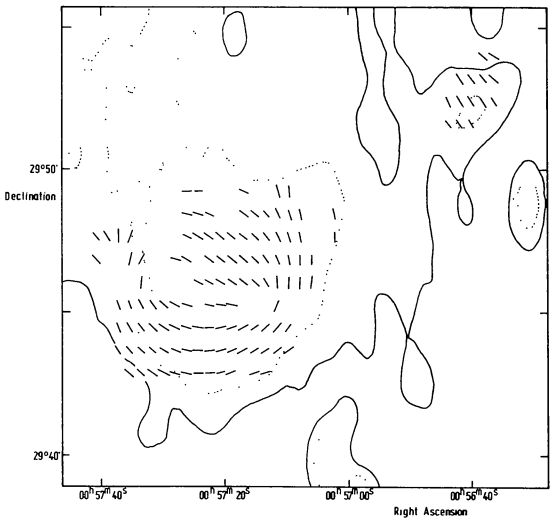

Fig. 5B: A low resolution (55" (α) x 110" (δ)) map of the magnetic field in the southeast lobe of NGC 315 superimposed upon contours corresponding to 4.5 and 15 mJy at 610 MHz (Gaussian beam restored map).

increased scatter in the RM near the radio core can probably be attributed to beam depolarization because the magnetic field near the nucleus in both the main and counter jets is known to change orientation on a scale considerably smaller than the 55"x110" beam used for the RM analysis (Fomalont et al., 1980).

Slow variations in RM of a few radians m^{-2} over an angular scale of a few arc minutes are similar to these found in the giant radio galaxies 3C326 (b = 48°) and 3C236 (b = 54°) (Papers I and II). We therefore believe that most (8-10 rad m^{-2}) of the RM variations in Figs. 4A and 4B are due to fluctuations in the galactic foreground rather than to variations internal to the source.

We have used the RM data and the 21 cm E-vectors to construct maps of the component of the magnetic field in NGC 315 projected perpendicular to the line of sight.

Because the region within 30" of the radio core is known to exhibit changes in the magnetic field orientation (Fomalont et al., 1980) we made a magnetic field map of the jets and northwestern lobe from the full resolution 21 cm E-vectors. This full resolution magnetic field map (shown in Fig. 5A) was made by combining two maps, one corrected for a RM of -78 rad m^{-2} and one corrected for a RM of -83 rad m^{-2}. We combined selected parts of each of these maps, based on the local RMs (shown in Fig. 4A), so that individual vectors in the resulting map should deviate from their intrinsic position angles by no more than $\sim 8°$ (corresponding to an offset of $\sim |3|$ rad m^{-2} RM).

The region of Fig. 5A near the center of NGC 315 shows the magnetic field transition documented at higher resolution by Fomalont et al. (1980); the dominant field component in the main jet is parallel to the jet for the first ~25 arcsec (~7.8 kpc) northwest from the core but changes to a well-ordered perpendicular configuration at greater distances. Figure 5A further shows that this perpendicular configuration persists in a highly organized form as far as ~970 arcsec (305 kpc) from the core where the jet begins to bend to the southwest. The figure also shows that for the first ~290 arcsec (91 kpc) of the counter jet southeast of the nucleus the field lies parallel to the jet at its edges, but perpendicular to the jet at its center. In these respects the magnetic field distribution in the jets of NGC 315 is closely similar to those of 3C31 (Fomalont et al., 1980; Burch, 1979b). In both cases the magnetic field in the brighter jet is parallel to the extension of the jet in the region near the radio core but subsequently changes to a predominantly perpendicular configuration. No such transitions can be seen in the fainter counter jets in either source. At large distances from the core of 3C31 the high-resolution observations of Fomalont et al. showed that both the main and counter jets have the field parallel at the edges and perpendicular at the center while in our observations of NGC 315 this phenomenon is evident only in the counter jet close to the core and possibly in the main jet about 16.4 arcmin from the core, just before it begins to bend to the southwest. In contrast to the situation in 3C31 where the degree of polarization in the parallel regimes at the edges of the jets is lower than found in the perpendicular regimes in the middle, in NGC 315 the degree of polarization in the field-parallel regime at the outer edge of the counter jet appears higher than that of the field-perpendicular regime at its center. This apparent drop in the degree of polarization in the middle of the NGC 315 jet could however be caused by beam depolarization.

The field structure in the northwest lobe also appears to have the parallel/perpendicular configuration. At the outer edges of the lobe the field runs parallel to the extension of the lobe. In the center of the lobe it is generally perpendicular, although there are deviations that could be associated with compressions of the radio emitting plasma and magnetic fields resulting in the local peaks of emission superposed on the general diffuse emission of this lobe (Fig. 2A).

At the 49 cm resolution, the magnetic field in the bright part of the southeast lobe has a loop-like circumferential structure (Fig. 5B) similar to that in the northern lobe of 3C219 (Perley et al., 1980) and the southern lobe of 3C382 (Strom et al., 1978; Burch, 1979a). Little additional detail is present in the 21 cm full resolution map of this lobe so we have not displayed it.

Because no polarized flux was detected in either of the CJ? features at 49 cm, we were not able to determine RMs and thus magnetic field orientations directly in either of these features. We have therefore assumed that the galactic foreground RM is -78 rad m^{-2} and -76 rad m^{-2} for the CJ? features closer and further from the nucleus respectively. These RMs correspond to the those measured in the southeast lobe and the counter jet in the regions closest to the CJ? features. The magnetic fields in these features (displayed also in Figs. 5A and 5B) were derived with the above RMs and 21 cm electric vectors. This procedure is justified as 11 cm E-vectors derived from the 21 cm E-vectors with the above RMs agree with those measured in these regions by Stoffel and Wielebinski (1978). The magnetic fields in the CJ? features also appear to be oriented perpendicular to the major axes of the features, further confirming their association with the counter jet structure.

II. Depolarization.

After convolution of the 21 cm data to the 49 cm resolution, we have compared the polarization data available for NGC 315 at the two wavelengths.

Before we directly compare the data, we must point out an instrumental effect which limits the

accuracy of our results. A zero level offset of ∿ 2.5 mJy (the actual value fluctuates from point to point within the maps) is present in the 21 cm total intensity maps when convolved to the 49 cm resolution. There are several reasons for this offset:

a) the 21 cm observations contained baselines increasing from 36 meters in increments of 18 meters. We are therefore missing the 18 m spacing and zero spacing from an ideal uniform array. In the convolved maps the missing contributions from the 0 and 18 m spacings are relatively more important, causing a large depression to appear. Also, the 21 cm observations of the jet and northwest lobe miss a 12 hour observation that had a shortest spacing of 72 meters (see Table 2) so the effects of missing short spacings are even more serious for that lobe.

b) Shadowing affects the observations made with 36 and 54 meter shortest spacings at extreme hour angles. The decrease in the amplitudes produced by shadowing at the extreme hour angles causes a large scale ripple over the maps in the north-south direction.

The presence of the zero offsets has two effects: a) the spectrum of the fainter emission appears too steep because the fainter emission at 21 cm will have a relatively lower apparent total intensity than the higher surface brightness features for which the small offset becomes relatively unimportant.

b) again, because the total intensity of the lower brightness features will be relatively too low, P_{21} will appear too high in low brightness regions (the offset problem is not significant for the polarized flux data), and consequently the measured 21 cm - 49 cm depolarization, P_{49}/P_{21}, will be too low.
Both effects are seen to some extent in the data and we made spectral index maps and depolarization maps both with and without offset corrections in order to examine their magnitudes. The following discussion relates only to properties which we believe to be real, after inspection of the corrected and uncorrected maps.

Fig. 6 shows the distributions of depolarization, degree of polarization and 49 cm total intensity along the ridges of the main and counter jets. The large scatter in the depolarization near the radio core source is due to beam smearing from the core plus a complicated blending (with the present resolution) of radiation that originated in parellel and perpendicular magnetic fields. However, at distances further than ∿60 arcsec from the core the depolarization in the main jet is essentially constant at about 0.8 ± 0.2. The depolarization in the counter jet apparently drops to ∿ 0.4 near $\alpha \sim 00^h55^m20^s$, $\delta \sim 30^\circ03'$, but this large depolarization is probably due to 49 cm beam depolarization; there is a difference of ∿4 rad m^{-2} in the foreground RM between positions northwest and southeast of $\alpha \sim 00^h55^m20^s$, $\delta \sim 30^\circ03'$ (see Fig. 4A) which will cause some vector cancellation to occur by 49 cm. At the outer end of the counter jet the depolarization is 0.8, similar to that in the main jet.

Depolarization is definitely present in the southeast lobe (Fig. 7) with a typical value again being ∿0.8. The data suggest that the depolarization is greatest in the center of the lobe near the total intensity peak with less depolarization occurring toward the outer edges.

Unfortunately it is not possible to make a quantitative analysis of the depolarization in the northwest lobe because of beam depolarization when the 21 cm data are convolved to the 49 cm resolution. It can be seen from the full resolution 21 cm E-vector map (Fig. 2C) that, at this wavelength, the polarization E-vectors at the outer parts of this lobe

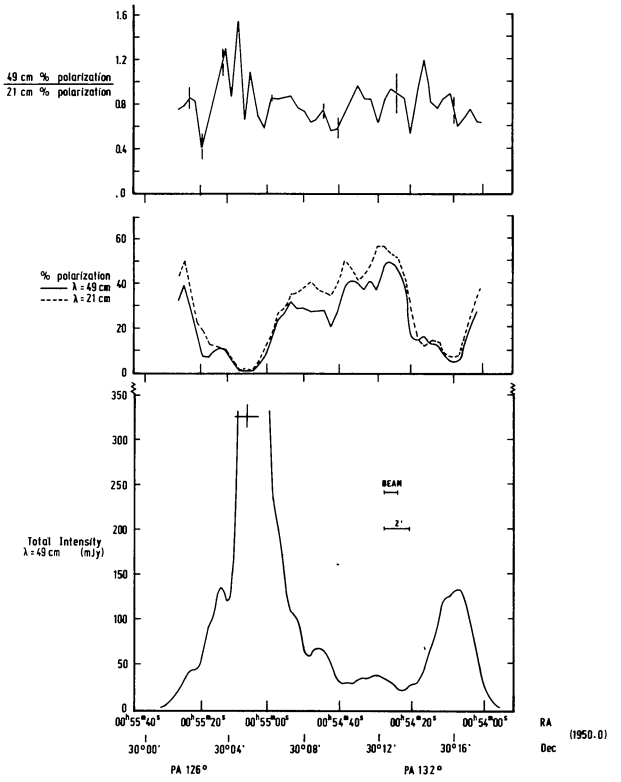

Fig. 6: A cross cut along the jet and counter jet of NGC 315 showing the depolarization between 1415 MHz (21 cm) and 610 MHz (49 cm). Error bars are plotted at representative sample points. Also plotted for reference are the 21 cm degree of polarization as seen when the data are convolved to 49 cm resolution and the 49 cm degree of polarization and total intensity. The cross marks the position of the central nuclear source.

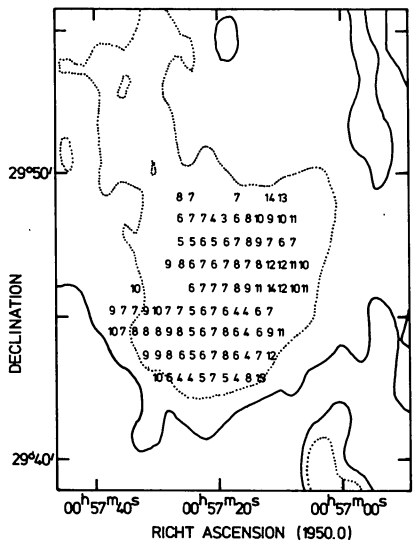

Fig. 7: The depolarization between 49 and 21 cm in the southeast lobe. Values are in units of one tenth, i.e. 6 equals 0.6. Contour values are the same as those for Fig. 3B.

are oriented roughly perpendicular to those at the center. Convolution of the data to the 49 cm resolution therefore leads to a considerable decrease in the apparent degree of polarization over this lobe because of increased E-vector cancellation. Corresponding beam depolarization does not occur at 49 cm because the distribution of RM over this lobe (Fig. 4A) is such that by 49 cm the E-vectors are roughly parallel over the lobe (Fig. 1C). Thus an analysis of depolarization over this lobe must await a 49 cm map with better resolution.

b) Spectral Variations over NGC 315.

Using Arecibo data at frequencies between 408 and 2700 MHz, Bridle et al. (1976) showed that the spectral index was fairly constant over NGC 315 between these frequency limits, with a mean value of -0.5 ± 0.2. The spectral indices derived between 49 and 21 cm from the present Westerbork data generally substantiate this conclusion although the present results are influenced by uncertainties in the 21 cm zero level offsets due to missing short spacings (0, 18 and, for the northwest lobe, 72 meters) at this wavelength.

Along the main and counter jets the 49 - 21 cm spectral index is constant at -0.6 ± 0.1 (Fig. 8). No significant deviations from this value occur along the jet itself. The radio core clearly has a much flatter spectrum as noted by Fanti et al. (1976) and Bridle and Fomalont (1978).

We computed two-dimensional spectral index maps over the northwest and southeast lobes together with "error maps" made assuming that the zero level offsets cause maximum brightness errors of ± 2.5 mJy/beam in the northwest lobe and ± 1.5 mJy/beam in the southeast lobe.

Figs. 9A and 9B display the spectral index distribution for that region of the northwest lobe where the calculated spectral index error, based on the above uncertainties, is less than ± 0.2. There appears to be significant spectral variation over this lobe. The spectrum is flattest ($\alpha \sim -0.4$) at the outer northern edge of the bright northern peak and steepens to a typical value of ~ -0.65 in the more southerly part of this lobe. Fig. 9B also suggests that at declinations lower than $30^{\circ}14'$ the spectrum steepens from west to east across the lobe. Typical values for the spectral index of -0.6 to -0.7 occur at the western edge (where the intensity gradient is sharpest) while values of -0.8 to -0.9 are found at the eastern edge (where diffuse emission is seen (Fig. 1A)). Because of the zero level offset problem discussed above, it would however be desirable to

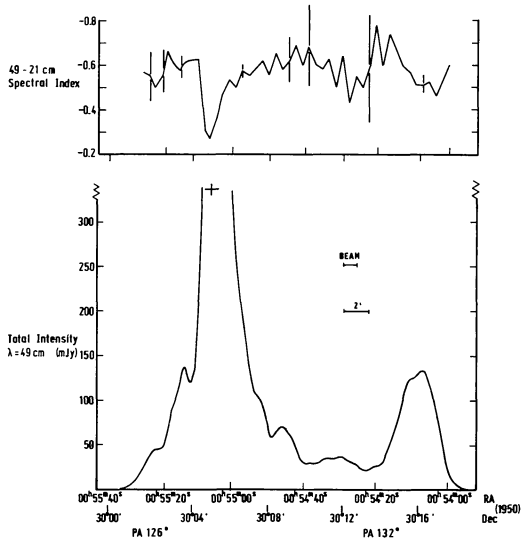

Fig. 8: A cross cut showing the distribution of spectral index (in the sense $S_{\nu} \propto \nu^{\alpha}$) along the jet and counter jet of NGC 315. For comparison purposes a cross cut through the 49 cm total intensity map is also shown.

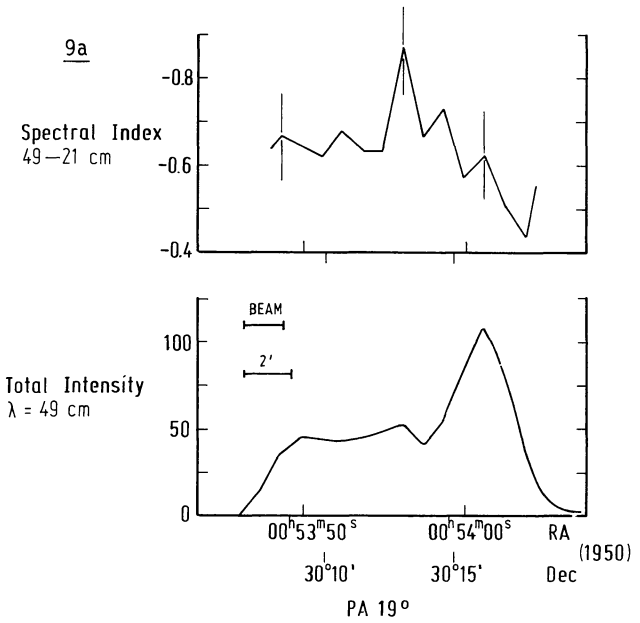

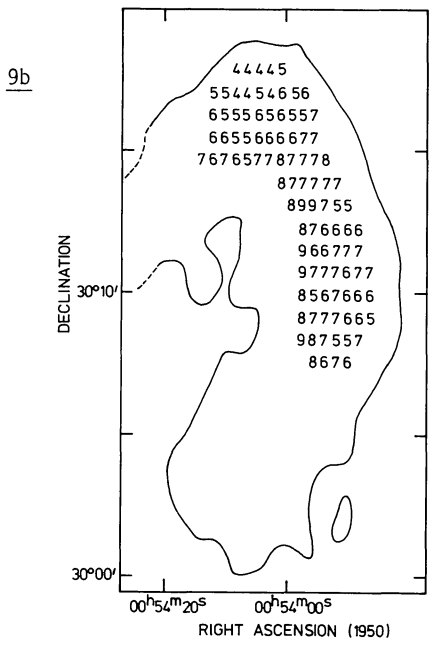

Fig. 9: The spectral index distribution over the northwest lobe. a) a cross cut through the center of the lobe in position angle 19°b) distribution of spectral variation over the lobe. Values are in units of -0.1, i.e. 6 equals a spectral index of $\alpha = -0.6$ ($S_{\nu} \propto \nu^{\alpha}$). The contour is the same as that for Fig. 3A.

confirm these spectral index variations by independent measurements.

In the southeast lobe the spectral index of the higher surface brightness regions was found to be constant at -0.6 to -0.7 with no obvious variations, so we have not presented the spectral index map in a figure.

4. Expansion angle and structure of the jet.

We measured the deconvolved half-intensity width (FWHM) of the jet and counter jet as a function of angular distance from the the central radio core by making cross cuts through the full-resolution 21 cm map in directions perpendicular to the extension of the jet and counter jet at increments of 30 arcsec distance from the radio core. The deconvolved half widths were computed by assuming the beam in the direction perpendicular to the jet to have a Gaussian half width (FWHM) of 31". The results from the analysis are displayed in Fig. 10; Table 2 lists mean expansion parameters for the jets based on the data shown in Fig. 10.

Consider first the expansion properties of the main jet. The present data, together with that of Bridle et al. (1979), show that the main jet can be separated into six different regimes:

1) the regime at an angular separation (θ) from the core of less than 7" ($\sim$2 kpc) where no radio emission greater than 1.6 mJy per beam was detected in the 6 cm VLA map of Bridle et al.,

2) the regime at $\theta > 7$" where the jet rapidly brightens but is unresolved in the VLA maps and thus has a FWHM angular width (Φ) $\lesssim$ 2" (600 pc) perpendicular to its extension,

3) the regime extending from $\theta \sim 15$" (5 kpc) to $\theta \sim 2'$ (38 kpc) in which the jet flares out at an average expansion angle [2 arctan $\frac{1}{2}d\Phi/d\Phi$] of $\sim 18^\circ$ (Table 2). Note however that the expansion rate ($d\Phi/d\Phi$), the expansion angle and the cone angle [2 arctan $\Phi/2\theta$], which is the angle subtended by the cross sectional width (FWHM) of the jet at the nucleus, all decrease with increasing θ in this regime. The jets in 3C31 have a very similar structure (Bridle et al., 1980a),

4) the regime beyond $\theta \sim 2$ arcmin (38 kpc) where the jet maintains a roughly constant width of $\Phi \sim 47$ arcsec (15 kpc) until

5) the regime $\theta > 420$" ($\sim$130 kpc) in which it again grows at a constant expansion angle of $\sim 10^\circ$ until a distance of $\sim$14.5 arcmin (270 kpc) from the nucleus is attained. Finally,

Table 2. Mean Expansion Parameters of the NGC 315 Jets.

	Angular Separation from Core θ(arcsec)	Angular FWHM of Jet Φ(arcsec)	Expansion Rate $(d\Phi/d\theta)=\mu$	Expansion Angle 2 arctan $(\mu/2)$	Cone Angle 2 arctan $(\Phi/2\theta)$
NGC 315 main jet	30	13	0.46	26	24
	60	26	0.38	21	24
	90	36	0.29	17	23
	120	43	0.17	10	20
	150	46	0.07	4	17
	180	48	0.06	3	15
	210	48	0.03	2	13
	240	49	0.01	0.5	12
	270	49	-0.01	-0.5	10
	300	48	-0.05	-3	9
	330	47	-0.05	-3	8
	360	46	-0.06	-3	7
	390	43	-0.08	-5	6
	420	43	0.17	10	6
	450	49	0.17	10	6
	480	54	0.17	10	6
	510	59	0.17	10	7
	540	64	0.17	10	7
	570	69	0.17	10	7
	600	74	0.17	10	7
	630	80	0.17	10	7
	660	85	0.17	10	7
	690	90	0.17	10	7
	720	95	0.17	10	8
	750	100	0.17	10	8
	780	106	0.17	10	8
	810	110	0.17	10	8
	840	116	0.17	10	8
	870	121	0.17	10	8
NGC 315 counter jet	30	20	0.54	30	37
	60	35	0.38	21	32
	90	44	0.22	13	27
	120	50	0.15	9	24
	150	54	0.10	6	20
	180	57	0.10	6	18
	210	60	0.08	5	16
	240	62	0.08	5	15
	270	65	0.07	4	14

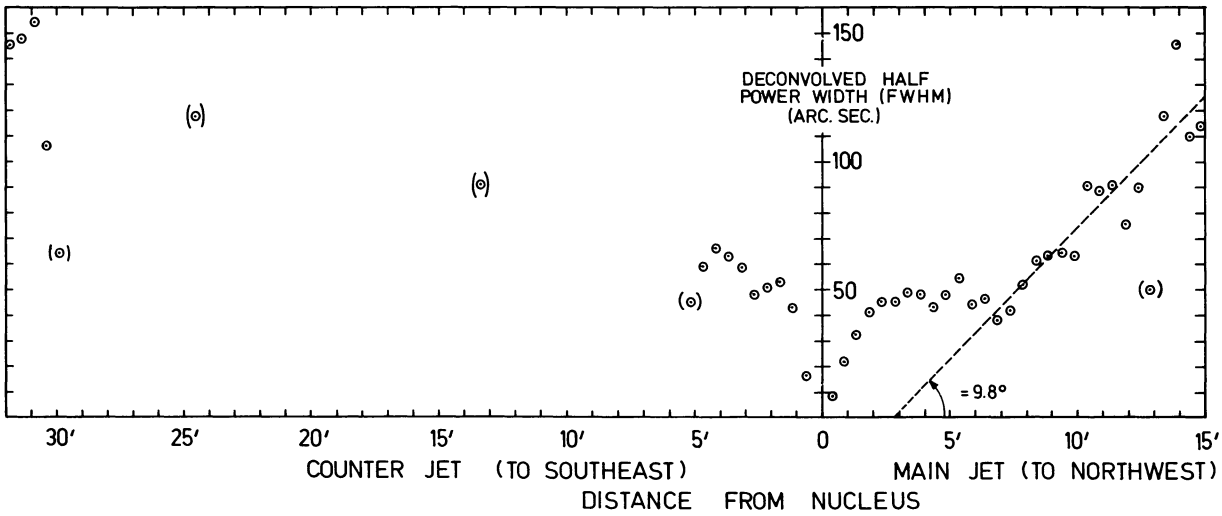

Fig. 10: Cross sectional widths of the jet and counter jet as a function of distance from the central nuclear source. A description of how the widths were derived is given in the text. The small brackets signify data that are probably of poor quality (low signal to noise, distortion by instrumental effects, etc.). The large brackets surround values which indicate "average" widths for the CJ? features. The dashed line is a least squares fit to the cross-sectional widths in the main jet at distances greater than 7 arcmin from the nucleus. The least squares fit corresponds to a constant opening angle of 9.8°.

6) beyond θ = 14.5 arcmin the surface brightness increases and the jet bends to form the northwest lobe.

The counter jet also exhibits an initial regime of rapid expansion within $\sim$1.5 arcmin from the core source which corresponds to that at similar distances from the core in the main jet. Beyond $\theta\sim$1.5 arcmin, the counter jet expands more slowly although it probably continues to expand out to $\theta\sim$5 arcmin from the nucleus where its emission dies out. This behaviour contrasts with that of the main jet which clearly ceases to expand between $\theta\sim$ 2 arcmin and 7 arcmin.

The two sample points enclosed in large brackets in Fig. 10 are estimates of the average widths of the two CJ? features. These suggest that the CJ? features have continued to expand at roughly the same expansion rate as the outer parts of the counter jet. Finally at $\theta\sim$ 31 arcmin we have measured a few half intensity (FWHM) widths in the part of the southeast lobe that is closest to the CJ? feature (where a hypothetical "beam" would be "hitting" the southeast lobe). These widths are also consistent with the counter jet continuing to widen at the same average rate until it becomes amalgamated into the southeast lobe. The evidence therefore suggests that after the rapid expansion phase at $\theta \lesssim$ 90" from the core, material associated with the counter jet expands at an approximately constant rate (with only slight 'focussing') until it blends into the southeast lobe at a projected distance of some 580 kpc from the radio core.

Focussing as the distance from the core increases would not be unexpected since the pressure within the jet should drop as it expands both because
a) the flow in the jet should become more ordered and
b) the internal density and temperature should decrease.
Consequently if the pressure in any surrounding intergalactic medium drops sufficiently slowly, it and the pinching effect of the organised transverse (circumferential) magnetic field may be better able to confine the jet as it opens out, until all pressures drop to those permitting an asymptotic free (ballistic) expansion. We discuss these collimation properties in terms of detailed models of the jet dynamics elsewhere (Bridle et al., 1980b; Willis et al., 1981).

5. Surface brightness variations of the jet and counter jet.

We saw earlier (Fig. 5A) that the organized component of the magnetic field in the jet and counter jet lies mainly perpendicular to the jet extension beyond 20" from the radio core. The transition from the parallel field at $\theta <$ 20" in the main jet to an organized perpendicular configuration further from the core suggests that over most of the jet and counter jet the dominant magnetic field component will be proportional to R^{-1} where R is the increasing cross-sectional width as predicted by Blandford and Rees (1974) in the absence of field-amplifying processes. As the jet expands, we also expect that the relativistic particle energies should decrease because of adiabatic losses unless there is particle reacceleration in the jet. Assuming the synchrotron emission to come from a filled jet, we should then expect the observed surface brightness, I, at the center of the jet to be proportional to $R^{(7\alpha-6)/3}$ where α is the spectral index. For $\alpha\simeq -0.6$ (Fig. 8), we would therefore obtain a surface brightness decrease of the form $I \propto R^{-3.4}$ in the absence of field or particle replenishment within the jets.

We have used our 21 cm total intensity map (Fig. 2A), the VLA 20 cm maps of Bridle et al. (1979), and an unpublished VLA 6 cm map of the innermost part of the main jet to plot the surface brightness of the jets as a function of jet width R which we equate here with the parameter Φ. The VLA 6 cm data were scaled to 21 cm assuming that the 21 cm - 6 cm spectral index remains -0.6 in the innermost part of the main jet. The results are displayed in Figs. 11A and 11B for the main and counter jets respectively. These figures clearly show that while the brightness of both jets does indeed decrease as the cross-sectional width increases, there is no constant power law relation between brightness and jet width that holds for the entire length of either the jet or counter jet.

In the inner ($\theta <$ 60", 19 kpc) regimes of rapid expansion in both the main and counter jets the VLA data show that the brightness falls off much more slowly than $R^{-3.4}$; a fit to the VLA points defining

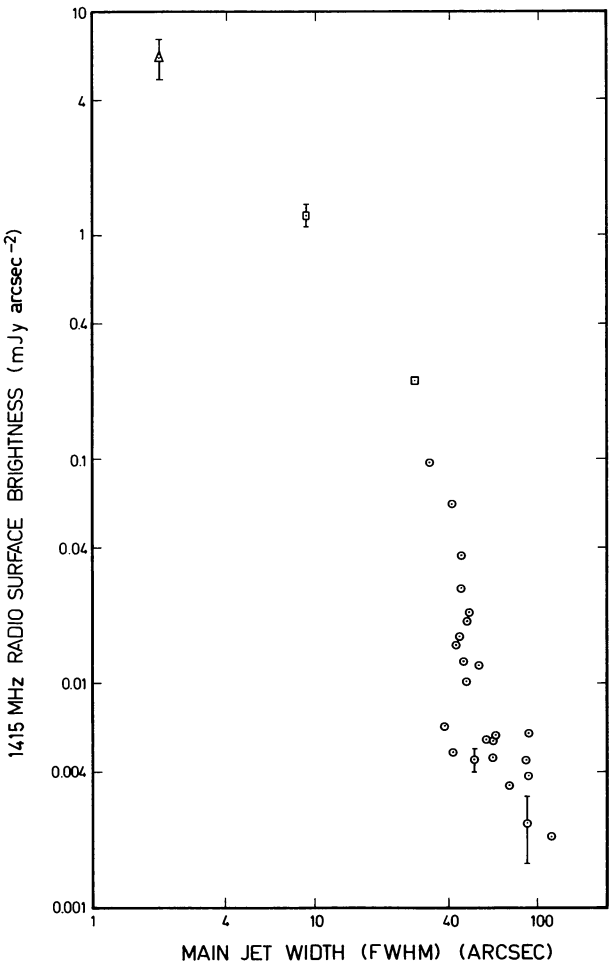

Fig. 11A: A logarithmic plot of 1415 MHz radio surface brightness as a function of deconvolved jet width (FWHM) for the main jet of NGC 315. The square boxes refer to data calculated from the VLA 21 cm maps of Bridle et al. (1979). The triangular box refers to data from an unpublished VLA 6 cm map and scaled to 1415 MHz with the assumption that the 21 cm - 6 cm spectral index of the innermost part of the main jet is -0.6. The rest of the data points are derived from cross-cuts through the WSRT 21 cm map shown in Fig. 2A.

the brightness in the main jet where it is less than 30" wide gives a brightness proportional to $R^{-1.25\pm0.12}$. Only one VLA point is readily available for the counter jet. It falls far below the brightness that would be expected if the brightness-width relationship for the outer part of the counter jet were to be extrapolated back to a smaller cross-sectional width. Thus the brightness-cross-sectional width relation for the inner part of the counter jet is probably very similar to that of the inner regime of the main jet. Therefore the data favor continuous replenishment of particles and/or fields in the inner regimes of rapid expansion in both the main and counter jets.

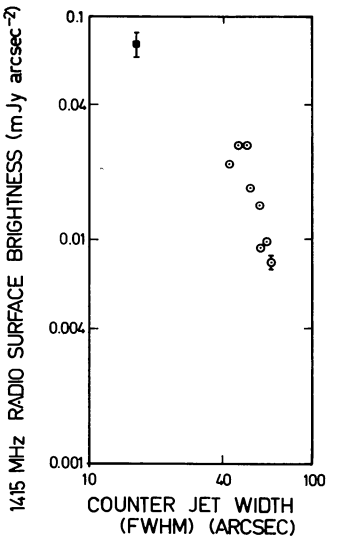

Fig. 11B: A similar plot of surface brightness vs. jet width for the counter jet.

The surface brightness in other regimes of the main and counter jets does, however, decrease much more sharply. In the main jet the surface brightness decreases by about an order of magnitude while the cross-sectional width varies from about 30 to 50 arcsec. This variation occurs in what was called regime 4) above - the region of roughly constant cross-sectional width where the distance from the nucleus increases from $\sim$2 to 7 arcmin. A least squares fit gives a surface brightness proportional to $R^{-4.42\pm1.10}$. Thus the slope is apparently steeper than that expected if magnetic flux conservation and adiabatic losses occur although the slope is not significantly "over-steep". In the outer part of the main jet, which is expanding at a constant expansion angle of $\sim10^{\circ}$ (Fig. 10), the data suggest that the brightness is again less dependent on jet cross-sectional width (a least squares analysis gives a fit proportional to $R^{-0.69\pm0.25}$) but the large individual uncertainties both in measured surface brightness and cross sectional width in this regime combine to make the result very uncertain. A fit to the entire regime at $\theta > 60"$ gives $I \propto R^{-2.31\pm0.42}$, which is roughly consistent with magnetic flux conservation and adiabatic losses.

The counter jet regime at $\theta\sim1.5$ to $\theta\sim5$ arcmin from the nucleus corresponds approximately to regime 4) of the main jet in that the rate of expansion is clearly much slower than in the regimes of rapid expansion lying within $\theta\sim1.5$ arcmin. In regime 4) of the main jet the surface brightness is very sharply dependent on the jet width (see above) so it is perhaps not surprising that similar behavior is present in this regime of the counter jet. Here the surface brightness is proportional to $R^{-2.94\pm0.65}$.

Thus in both the main and counter jets the surface brightness drops off most sharply as a function of jet width in those regimes where the rate of jet expansion is low and vice versa. In the jet regimes having the most rapid rate of expansion the surface brightness falls off more slowly than would be expected on the basis of magnetic flux conservation and adiabatic losses; in the regimes having lower rates of expansion the surface brightness dependence on jet width is, however, consistent with that expected to within the nominal least squares errors.

6. Minimum Energy parameters of NGC 315.

We have used the present data, the VLA 20 cm maps of Bridle et al. (1979) and the high resolution unpublished VLA 6 cm map to compute integrated surface brightnesses, I_{int}, over the range 10^7 to 10^{10} Hz, assuming a constant spectral index of -0.6 over this frequency range. If we assume that conditions near equipartition hold then we can derive the energy minimizing magnetic field strength B_{min} from the integrated surface brightness by (Perley et al., 1979),

$$B_{min} = \left[\frac{6\pi K' I_{int} (1+k)}{L |\sin\psi|^{3/2}}\right]^{2/7}$$

where L is the path length through the source which we have assumed equal to the observed widths, k is the ratio of the energy in protons to electrons which we have assumed equal to unity and K′ is essentially constant (see Perley et al., 1979). ψ is the angle between the line of sight and the magnetic field, which we have assumed $\sim90^{\circ}$.

The internal energy density in particles and fields is then given by

$$U_{min} = \frac{7 B_{min}^2}{24 \pi}$$

Results for various locations over the radio source, marked in Figs. 2A and 2E, are listed in Table 3. The values for the magnetic field strength and the energy density in NGC 315 are very similar to those found for other large radio galaxies such as 3C326 (Willis and Strom, 1978) and 3C236 (Strom and Willis, 1980).

The magnetic field at the sample locations listed in Table 3 clearly decreases as the jets widen. However, any further interpretation must be done cautiously because of

a) the dependence of the calculated field strength on the surface brightness, assumed depth through the source and assumed ratio of proton to electron energies,

b) the assumption of conditions near equipartition.

There may be departures from equipartition in those regimes of the main and counter jets where we have the brightness dependence on jet width in accordance with that expected if the magnetic flux is conserved and the relativistic particles suffer adiabatic losses.

The magnetic field energy density, $B^2/8\pi$, will be proportional to R^{-2} if B is proportional to R^{-1} in those regimes. However, if the relativistic particles are also undergoing adiabatic losses then the energy density of the relativistic particles should be proportional to $R^{-\frac{8}{3}}$. Thus if the equipartition conditions exist within these regions at some given

Table 3. Some Physical Parameters for Various Locations in NGC 315.

NGC 315 redshift 0.0167 (Colla et al., 1975)

Luminosity Distance 67 Mpc

(H_o = 75 km s^{-1} Mpc^{-1})

Luminosity at 49 cm ~4 x 10^{24} watt Hz^{-1}

Luminosity (10^7-10^{10} Hz) ~2 x 10^{34} watt

Size conversion ratio 1 arcsec = 314 pc

Location	Distance to Nucleus (arcsec)	Width(=depth) of feature (FWHM) (arcsec)	Integrated Brightness (erg cm^{-2} s^{-1} sr^{-1})	B_{min} (μgauss)	U_{min} (erg cm^{-3})
Main jet.					
1 *	12	~2	1.9×10^{-5}	31	9.1×10^{-11}
2 *	24	~9.1	3.9×10^{-6}	13	1.6×10^{-11}
3 *	73	~28	6.9×10^{-7}	5.7	3.0×10^{-12}
4	132	~44.5	1.2×10^{-7}	3.0	8.4×10^{-13}
5	342	~47.5	4.7×10^{-8}	2.3	4.8×10^{-13}
6	450	~50	1.3×10^{-8}	1.6	2.3×10^{-13}
7	749	~100	4.4×10^{-9}	0.94	8.1×10^{-14}
8	1037	~150	5.8×10^{-8}	1.7	2.8×10^{-13}
Counter-jet.					
A *	40	~16	2.3×10^{-7}	4.9	2.2×10^{-12}
B	144	~50	8.7×10^{-8}	2.7	6.7×10^{-13}
C	281	~59	2.7×10^{-8}	1.8	3.0×10^{-13}
D	~ 840	~91	2.9×10^{-9}	0.9	6.8×10^{-14}
E	~ 1470	~118	3.3×10^{-9}	0.8	6.3×10^{-14}
Northwest lobe.					
9		~180	1.0×10^{-8}	1.0	9.4×10^{-14}
Southeast lobe.					
F		~350	2.4×10^{-8}	1.1	1.0×10^{-13}
G		~100	1.0×10^{-8}	1.2	1.3×10^{-13}
H		~375	2.1×10^{-9}	0.43	1.7×10^{-14}

* Parameters at these locations are from the VLA maps.

distance from the radio core then we expect there will be departures from equipartition elsewhere because of changes in the jet width and the different power law dependences given above.

7. Depolarization and thermal particle densities in NGC 315.

One of the most striking aspects of the NGC 315 jets is the near constancy of the 49 cm/21 cm depolarization ratio at 0.8 ± 0.2 (Fig. 6). For a simple slab model of depolarization, Burn (1966) gives the complex degree of linear depolarization, P, as a function of wavelength λ, by

$$P(\lambda^2) = P_i \frac{1-e^{-s}}{s}$$

where P_i is the observed intrinsic degree of polarization (we assume P_i equals the degree of polarization in the 21 cm convolved maps: beam depolarization will make this value too low in some regions such as location B in the counter jet). In this expression

$$s = (KnB_r)^2 dL\lambda^4 - i2KnB_L L\lambda^2$$

where L = the path length through the source, n = thermal particle density and K is a constant. B_L and B_r are the uniform component of magnetic field along the line of sight and the random component of magnetic field respectively. d is a scale length for the random field fluctuations. B_L and B_r are estimated from $B_L \sim (\frac{1}{3}\frac{P_i}{P_\gamma})^{\frac{1}{2}} B$ and $B_r \sim \{B^2 - B_o^2\}^{\frac{1}{2}}$

where B = total magnetic field and B_o = total uniform field.

$$B_o \sim \{3B_L^2\}^{\frac{1}{2}}$$

P_γ(~72%) is the maximum possible degree of linear polarization, given an isotropic distribution of relativistic electron pitch angles and a completely uniform magnetic field. Burn showed that the imaginary or real part of s will be dominant depending on whether N(=L/d, the number of fluctuation cells along the line of sight) is greater or less than ~$(B_r/2B_L)^2$ respectively. Since, at least at distances along the jets from the core greater than ~ 2 arcmin, $(B_r/2B_L)^2$ is roughly unity or less (Table 4) depolarization along the jets should be dominated by the imaginary component in the expression for s. The depolarization can then be described by

$$\frac{P_{49}}{P_{21}} = \frac{\sin x}{x}$$

where P_{21} equals the intrinsic degree of polarization and $x = KnB_L L\lambda^2$. (This argument may not hold for the peak at location 8 (Table 4) where the main jet bends to the southeast but it is true along the straight parts of the main and counter jets.) Using the sin x/x

Table 4: Depolarization Parameters for Various Locations in NGC 315.

Location	Intrinsic Degree of Polarization	$\frac{P_{49}}{P_{21}}$	B_L (μgauss)	$\left(\frac{B_r}{2B_L}\right)^2$	Density of Thermal Material (cm^{-3})
Main Jet.					
4	24	0.85	1.0	1.47	4×10^{-4}
5	38	0.71	1.0	0.65	5×10^{-4}
6	48	0.69	0.8	0.36	6×10^{-4}
7	45	0.86	0.4	0.43	4×10^{-4}
8	8	0.64	0.3	5.91	6×10^{-4}
Counter-jet.					
B	13	1.0	0.7	3.35	?
C	43	0.85	0.8	0.49	3×10^{-4}
Southeast Lobe.					
F	27	0.7	0.4	1.22	~2×10^{-4}
G	56	0.9	0.6	0.20	~2×10^{-4}

expression and the local values of the P_{49}/P_{21}, values of the density of thermal depolarizing material at various locations in NGC 315 were calculated (see Table 4). Note that the value for the magnetic field along the line of sight, B_L, was calculated with the assumption that B, the total magnetic field, has the minimum energy value (Table 3). Table 4 shows that there is very little scatter in the derived thermal particle density. Along the jet and counter jet the values all agree to within a factor 2 and n is about $4\times10^{-4}\,cm^{-3} \pm 2\times10^{-4}$.

Since a typical depolarization data point has an uncertainty of 0.1 to 0.2 (Fig. 6), any value of $Kn B_L L\lambda^2$ is uncertain by a factor of about 1.4. In addition the values of L and B_L at any location are derived on the basis of uncertain physical and geometrical assumptions so the values of thermal particle densities listed in Table 4 have individual uncertainties of at least 50%. Consequently they are not significantly different from each other.

Actually the most valid conclusion that we can make is that the depolarization is approximately constant at 0.8 everywhere along the jets. Then, assuming the depolarization to be described by the sin x/x law, we have $Kn B_L L\lambda^2 \sim 1.1$ radian at 49 cm, or

$$nB_L L \sim 1.8\times10^{-17} \text{ gauss cm}^{-2} = \text{const.}$$

If it can be confirmed with less noisy depolarization data that the density of the thermal material is indeed constant along the jet, an interesting physical situation arises. If v is the flow velocity along the jet and A is the cross-sectional area, we can define the mass flux along the jet as

$$\dot{M} \propto n\, v\, A$$

Noting that $A \propto L^2$ we can combine this with the condition above to obtain

$$\dot{M} \propto \frac{vL}{B_L}$$

Furthermore, if magnetic flux is conserved (as suggested by the transition in the jet from a region where the parallel field component dominates to one where the perpendicular one does) $B_L \propto L^{-1}$ which gives

$$\dot{M} \propto v\, L^2$$

Unless v decreases along the jet so as to compensate the L-dependence, M must therefore increase along the jet. This means either that more material was leaving the nucleus in the past, or gas becomes entrained along the length of the jet. An alternative that is marginally compatible with our data is that $P_{49}/P_{21} = 1.0$ so that $n \sim 0$ all along the jet.

8. The Gaps in the Counter Jet.

The counter jet consists of several sections of detectable emission separated by gaps (see Figs. 1A and 2E). There are various possible explanations for these gaps. Many double radio sources lack detectable jets yet are presumed to be energised by continuous beams, while some sources exhibit jets only on one side of the central object. It has been suggested (e.g. Turland, 1975) that these phenomena are manifestations of differing efficiencies of energy transport from the central objects to the extended radio lobes. Efficient beams would produce little radio emission and would therefore be difficult to detect as jets. In the context of these ideas, the gaps in the counter jet could be interpreted as regions where little energy is being radiated towards the observer at radio wavelengths although the flow of energy to the southeastern lobe is still streaming through them. Several phenomena might contribute to fluctuations in efficiency along a beam, including fluctuations in the strength of the magnetic field along the beam, fluctuations in the fraction of the beam energy resident in relativistic particles, and pitch-angle scattering of streaming particles by field inhomogeneities.

It is surprising however that there should be as many as three gaps in the counter jet while the main jet can be traced continuously from the nucleus of NGC 315 into the northwestern lobe. If the main jet is foreshortened by projection effects (as we suggest in Sect. 9 below) then it is possible that "gaps" in it are less evident due to partial merging with bright regions in projection. An alternative interpretation, however, is that the gaps in the counter jet represent significant decreases in the total rate of energy transport to the components, recording fluctuations in the energy output of this side of the central collimator during the time taken for material to travel the length of the counter jet. The absence of similar gaps in the main jet might then be attributed at least partly to differences between the nozzle conditions and flow velocities on the two sides of the central collimator. Unfortunately all such interpretations must remain highly speculative until convincing models are available for the contents and dynamics of the underlying beams.

9. The Large-scale Structure of NGC 315.

We now consider why the northwestern lobe of the extended structure appears nearly twice as close to the center of NGC 315 as does the southeastern lobe. Such asymmetries are not uncommon in very large radio galaxies (similar disparities were found in both 3C326 and 3C236 - papers I and II). A possible explanation is that in such large sources the material forming the lobes has entirely left the region of the circumgalactic medium that is dominated by the presence of the parent galaxy, so that the configuration of the lobes reflects chance asymmetries in the distribution of truly intergalactic material around the parent galaxy.

In the case of NGC 315 we suggest that the cause of the apparent asymmetry may be found not in the intergalactic medium itself but in the motion of NGC 315 through it. Indeed, the gradual large-scale "C" shaped curve of the jet and counter jet could be understood if these jets are the projection of a curved "twin-trail" structure such as that of NGC 1265 (Miley, 1976) bent behind the parent optical galaxy as it moves through the intergalactic medium. If NGC 315 is in motion then we can suggest the following possibilities to explain the large-scale asymmetry of this radio source.

First, if the structure of the source in three dimensions is in fact such a pair of symmetric curved trails, then the apparent foreshortening and brightening of the main jet could be attributed to this trail lying more nearly tangent to our line of sight than the counter jet, which would be oriented roughly perpendicular to the line of sight. This explanation requires that NGC 315 have a major component of its motion toward the northwest on the plane of the sky. It would then appear to overtake the northwestern component while leaving the southeastern one behind. If the two components are boring into an external medium at velocities V_{nw} and V_{se}, and the velocity of the galaxy along the line

joining them is V_g, then to explain the observed asymmetry we should require $V_g=(2\ V_{nw}-V_{se})/3$. If the Alfvén velocity in the outer components is of the same order as their velocities in the external medium, then V_g need only be of order a few hundred km/sec to account for the observed asymmetry. This is not unlikely if NGC 315 is a member of the Zwicky cluster (0107.5+3212) within whose boundary it appears to lie.

Second, as the galaxy moves through the intergalactic medium, either a secondary orbital motion of the galaxy, or precession of the central nuclear collimator (Bridle et al., 1976; Miley, 1976; Ekers et al., 1978) could produce the rotational Z-symmetry of the outer lobes. With such an interpretation, the northwestern "lobe" bending back to the south and east and finally ending at the large patch of diffuse emission south of NGC 315 would delineate the path traced out by the end of the jet in the past. The fact that the magnetic field structure of the northwestern lobe is parallel to the extension of the lobe at its edges but perpendicular to its extension along the central ridge is consistent with this interpretation as this is the magnetic field configuration found in the well resolved jet of 3C31 (Fomalont et al., 1980) and in the brighter part of the counter jet of NGC 315. This interpretation would imply that the large diffuse patch of emission to the south of NGC 315 is probably a remnant of earlier activity and that its apparent connection to the jets (Fig. 1) is partly an accident of projection.

High frequency spectral-index maps of the structure based on single-dish data would greatly assist evaluation of such interpretations of the gross morphology of the source by providing constraints based on the radiative lifetimes of the particles in different parts of the observed structure.

Acknowledgements.

The Westerbork Synthesis Radio Telescope is operated by the Netherlands Foundation for Radio Astronomy (SRZM) with the financial support of the Netherlands Organization for the Advancement of Pure Research (Z.W.O.). A.H.B. gratefully acknowledges receipt of an operating grant from the Natural Sciences and Engineering Research Council of Canada, and thanks the National Radio Astronomy Observatory and the University of New Mexico for their hospitality during the later stages of this work. A.G.W. would also like to acknowledge partial support from NSF grant AST 77-22906 while he was at Brandeis University. We thank P.P. Kronberg for communicating rotation measure data in advance of publication and A.G. de Bruyn for permitting us to use his deep optical plates. G. Beugel and W. Smit typed the manuscript while H. Meijer was responsible for photographic work.

References.

Blandford, R.D., Rees, M.J., 1974, Monthly Notices Roy. Astron. Soc. 169, 395.

Bridle, A.H., Davis, M.M., Fomalont, E.B., Lequeux, J., 1972, Astron. J. 77, 405.

Bridle, A.H., Davis, M.M., Meloy, D.A., Fomalont, E.B., Strom, R.G., Willis, A.G., 1976, Nature 262, 179.

Bridle, A.H., Fomalont, E.B., 1978, Astron. J. 83, 704.

Bridle, A.H., Davis, M.M., Fomalont, E.B., Willis, A.G., Strom, R.G., 1979, Astrophys. J. Lett. 228, L9.

Bridle, A.H., Henriksen, R.N., Chan, K.L., Fomalont, E.B., Willis, A.G., Perley, R.A., 1980a, Astrophys. J. Lett. 241, L145.

Bridle, A.H., Chan, K.L., Henriksen, R.N., 1980b, Journal Roy. Astron. Soc. Canada (in press).

Burch, S.F., 1979a, Monthly Notices Roy. Astron. Soc. 186, 519.

Burch, S.F., 1979b, Monthly Notices Roy. Astron. Soc. 187, 187.

Burn, B.J., 1966, Monthly Notices Roy. Astron. Soc. 133, 67.

Colla, G., Fanti, C., Fanti, R., Gioia, I., Lari, C., Lequeux, J., Lucas, R., Ulrich, M.H., 1975, Astron. Astrophys. Suppl. Series 20, 1.

Davis, M.M., 1967, Bull. Astron. Inst. Neth. 19, 201.

Ekers, R.D., Fanti, R., Lari, C., Parma, P., 1978, Nature 276, 588.

Fanti, R., Lari, C., Spencer, R.E., Warwick, R.S., 1976, Monthly Notices Roy. Astron. Soc. 174, 5p.

Fomalont, E.B., Bridle, A.H., Willis, A.G., Perley, R.A., 1980, Astrophys. J. 237, 418.

Hogbom, J.A., 1974, Astron. Astrophys. Suppl. Series 15, 417.

Hogbom, J.A., Brouw, W.N., 1974, Astron. Astrophys. 33, 289.

Miley, G.K., 1976, Proc. NATO Summer School, Physics of Non-Thermal Radio Sources, G. Setti (ed.), D. Reidel Publishing Co., p. 1.

Perley, R.A., Bridle, A.H., Willis, A.G., Fomalont, E.B., 1980, Astron. J. 85, 499.

Perley, R.A., Willis, A.G., Scott, J.S., 1979, Nature 281, 437.

Saslaw, W.C., Tyson, J.A., Crane, P., 1978, Astrophys. J. 222, 435.

Someren Greve, H.W. van, 1974, Astron. Astrophys. Suppl. Series 15, 343.

Stoffel, H., Wielebinski, R., 1978, Astron. Astrophys. 68, 307.

Strom, R.G., 1972, Netherlands Foundation for Radio Astronomy, Internal Technical Report No. 99.

Strom, R.G., Willis, A.G., 1980, Astron. Astrophys. 85, 36.

Strom, R.G., Willis, A.G., Wilson, A.S., 1978, Astron. Astrophys. 68, 367.

Turland, B.D., 1975, Monthly Notices Roy. Astron. Soc. 172, 181.

Vinokur, M., 1965, Annals d'Astrophys. 28, 412.

Wardle, J.F.C., Kronberg, P.P., 1974, Astrophys. J. 194, 249.

Willis, A.G., Perley, R.A., Bridle, A.H., 1981, in preparation.

Willis, A.G., Strom, R.G., 1978, Astron. Astrophys. 62, 375.